ARTICLE

Study of the mechanism of embolism removal in xylem vessels by using microfluidic devices

Guo Lihua [a], Yuanchang Liu [b], Li Liu [a], Liu Chong [a] and Li Jingmin [*a]

Determining the mechanism that effects embolism repair in the xylem vessels of plants is of great significance in predicting plant distribution and the screening of drought-resistant plants. However, the mechanism of perforation plates of xylem vessels in the acceleration of embolism repair is still not clear by using conventional methods of anatomy and visualization technology. Microfluidic devices have shown their ability for simulating physiological environment and conducting quantitative experiments. This work proposes a biomimetic microfluidic device to study the mechanism of perforation plates of xylem vessels in the acceleration of embolism repair. The results proffered that the perforation plates increase the rate of embolism removal by increasing the pressure differential through the vessel, and the rate of embolism removal is related to the structural parameters of the perforation plate. A combination of the perforation size, the vessel diameter and the perforation plate angle can be optimised to generate higher pressure differentials, which can accelerate the process of embolism repair. This work provides a new method for studying the mechanism of microstructures of natural plants. Furthermore, the mechanism that perforation plates accelerate embolism repair was applied to an electrochemical flow sensor for online determination of heavy metal ions. Test results of this application indicates that the mechanism can be applied in engineer field to solve the problems of reduced sensitivity of devices, inaccuracy of analysis results and poor reaction performance caused by bubbles that are generated or introduced easily in micro devices, which paves the way for applying the theory to engineer.

Introduction

Throughout recent decades droughts have caused rapid increase in global tree mortality and have had a negative impact on the function of ecosystems and carbon balance[1]. Tree mortality is projected to increase by up to 140% with a 4°C increase in average global temperature[2]. Climate models predict severe droughts on the regional scale in the future, which will fundamentally alter forest composition and distribution in many regions[3]. Embolism removal is the ability of plants to restore water transportation after encountering droughts and air embolisms can form easily in xylem vessels (henceforth referred to as vessel or vessels) under drought conditions[4]. The drought resistance of a particular type of plant is closely related to the ability and capacity of that plant to perform or undergo embolism removal of the vessels[5, 6]. This embolism removal mechanism can be used as a basis or factor for selecting suitable tree species for afforestation as well as providing a useful tool for predicting forest decline under drought conditions[7].

[a.] Key Laboratory for Micro/Nano Technology and System of Liaoning Province, Dalian University of Technology, Dalian, China.
[b.] Department of Mechanical Engineering, University College London, Torrington Place, London WC1E 7JE, UK
† E-mail: jingminl@dlut.edu.cn;

By researching the capacity for embolism removal to restore the water transportation in vessels, several studies have shown that perforation plates play an important role in embolism removal for vessels[8-13]. However, most of these studies were carried out under the remit of botany, where the research methodologies have been undertaken as anatomy and visualization, with the most significant results being vascular morphology and physiology[8, 14-16].

Previous studies have used anatomy, numerical simulation and visualization technology, including magnetic resonance imaging[17, 18] and X-ray imaging techniques[15, 16], to study perforation plates morphology[8, 14], their effect on improving hydraulic resistance[19, 20] and the water refilling process[12, 21]. The results show that perforation plates can trap air bubbles[22-25] and prevent them from spreading to adjacent vessels or aggregating into larger bubbles[8, 26, 27]. These studies assume that perforation plates act as a means of pressure control [28-30] that could speed up the process of embolism removal by increasing water pressure and promote the dissolution of air bubbles[31]. However, despite the broad observation and experiments to study embolism removal, the way in which perforation plates improve the process of embolism removal is still unresolved and the relationship between perforation plate morphology and the process of embolism removal remains to be seen. The research methods can't provide quantitative conditions for studying the influence of various factors on embolism removal.

Microfluidic devices can provide microenvironments similar to that in vessels of plant. In an effort to better understand this effect, this work proposes a mathematical model and a microfluidic device to study the mechanism by which perforation plates accelerate the process of embolism removal in vessels. Biomimetic microchannels fabricated by micro-nano technology were employed to investigate the relationship between the perforation plate morphology and the embolism removal performance. A mathematical model was created to analyse the relationship between pressure differential and embolism removal performance. Simulations were carried out to quantify the influence of the perforation plate composition on the pressure differential within the vessel. The study results of theoretical analysis, simulation and experiment show that the perforation plate can accelerate embolism removal by increasing the pressure differential, and rate of the embolism removal is related to the perforation width, perforation plate angle and vessel diameter. It is known that increase in pressure differential in the vessels can reduce the hydraulic efficiency, therefore determination of realistic and practical geometric parameters of the perforation plate are a trade-off between embolism removal performance and hydraulic efficiency. This work provides a new method for studying the mechanism of microstructures of natural plants by using microfluidic devices. More precise understanding of the mechanism of embolism removal in vessels of plants is of great significance when used for predicting plant distribution and screening drought-resistant plants. Furthermore, the mechanism by which perforation plates accelerate embolism removal in vessels can be applied to microfluidic devices to eliminate interference caused by bubbles. An electrochemical flow sensor with bionic unit was designed and tested to confirm it.

Materials and methods

Plant material

Branches of Platanus acerifolia were collected from Dalian University of Technology, located in the northeast of China. Branches were sealed in moist plastic bags and brought to the laboratory. After being cut into slices with length of 10 cm and thickness of 1 mm, samples were fixed in FAA for 24 hours. These samples were dehydrated in a series of ethyl alcohol solutions with concentrations of 50%, 70%, 95% and 100% each for 5 min. The samples were then lyophilized. Samples were fixed on an aluminum stub with double-sided electron conductive carbon cement and coated with gold. Samples were observed with a scanning electron microscope (SU8220, Hitachi High Technologies Corp., Tokyo, Japan) at an accelerating voltage of 5 kV.

Numerical approach

To analyze the role that perforation plates play in the embolism removal process of a vessel, a numerical simulation was conducted by using ANSYS FLUENT software. The CFD model is shown in Supplementary Fig. S1. The model was constructed at the same scale as the vessel of the angiosperm. The simulation conditions were set as pressure-implicit with splitting of operators (PISO). Mesh evaluation was performed to ensure that the results were not mesh dependent.

Fabrication of the biomimetic device

The biomimetic device was made from polydimethylsiloxane (PDMS) and it was fabricated by soft lithography technology. The SU-8 mold used for patterning was fabricated by using a photolithography technique (Supplementary Fig. S3). To hold the liquid PDMS, the SU-8 mold was assembled with an aluminum frame. Liquid-phase PDMS mixed by a base and curing agent in a 10:1 ratio (Sylgard 184, Dow Corning, USA) was poured into the SU-8 mold and degassed for 5 minutes. Then, it was baked at 85 °C in a vacuum oven (HMDS-2, CETC, China) for 1.5 hours. After being cured, the substrate was obtained by peeling off the PDMS from the SU-8 mold. The cover was fabricated by soft lithography technology without patterning. The biomimetic device was obtained by bonding the substrate and the cover by plasma etching technology (K1050X, Quorum, UK).

Measuring equipment

In the experiments conducted for this paper, the temperature of the solution and the surroundings was 25 °C. The water injection system contains a precision syringe pump (70-2001, Harvard, America) and a medical plastic syringe (10 ml, ZYMM, China). Gas flow in the experiment was controlled by a constant pressure pump (WH-PMPP-15, Wenhao Co., China). The pressure differential across the biomimetic device was monitored in real time by two pressure sensors. All of these devices were connected by polytetrafluoroethylene (PTFE) pipes. The image acquisition system was built with a microscope with a digital camera (IX71, Olympus, Japan), a data-acquisition card and a computer. Image Pro-plus software was used to analyze images. Data in this paper are presented as the mean ± standard deviation (SD).

Fabrication of the electrochemical flow sensor

To reduce interference caused by air bubbles and detect heavy metal contamination in water accurately, an electrochemical flow sensor consisting of a bubble removal unit and a detection unit was fabricated. The sensor consists of a cover and a base. The cover contains a bubble removal unit and a water sample holder. The base contains a substrate and three electrodes. The cover was made from PDMS and fabricated by soft etching technology. The substrate was made from glass. During the fabrication process, a titanium layer of 50 nm was sputtered on the glass to strengthen the adhesive capability between the gold electrodes and glass. Subsequently, a gold layer of 200 nm was sputtered on the titanium layer. After photolithography and corrosion, working and counter electrodes were obtained. The reference electrode was obtained by coating Ag/AgCl paste on the gold layer. Finally, the electrochemical flow sensor was obtained by bonding the PDMS cover and the base.

Procedure of heavy metal contamination detection by electrochemical flow sensor

Before the start of the experiment, copper solution was prepared by diluting the standard stock solution (500 mg/L, Copper standard solution, Aladdin) and KCl (0.1 M) in an acetate buffer solution (ABS). Differential pulse anodic stripping voltammetry (DPASV) was employed to measure the concentration of the copper ion solution. The detection procedure of heavy metal contamination by using the electrochemical flow sensor includes three steps. The first step is the electrochemical accumulation of copper ions. The copper ion solution containing bubbles was injected continuously into the electrochemical flow sensor at a flow rate of 400 μl/min for 70 s while a deposition potential of -0.05 V (vs. Ag/AgCl) was continuously applied at the electrodes. The second step is determination of copper ions. In this step, sample supply was halted and the deposition potential was removed. After a quiescent period of 30 s, differential pulse voltammetry (DPV) was applied to the electrodes with a potential ranging from -0.1 V to 0.4 V, amplitude of 25 mV and pulse width of 0.02 s. The differential pulse voltammogram was then obtained. The third step was removal of copper ions. Before the start of the next measurement, a potential of 0.6 V

was applied to the electrodes for 400 s while an acetate buffer solution was injected into the inlet at a flow rate of 200 μL/min. This step was used to remove any residual copper left on the surface of the working electrode. Each experiment was repeated three times. The blank sample, without copper ions, was also tested. The analytical signal was obtained by extracting the difference between the peak currents of the cooper sample and the blank sample.

Results and discussion

The mechanism by which perforation plates accelerate embolism removal

Water transported in vessels under negative pressure (Fig. 1a) is prone to embolism[32-34]. Air bubbles can inflate and expand rapidly to the entire vessels under negative pressure. In this condition, the number of vessels used for water transportation decreases, which leads to significant decline in hydraulic efficiency. Decline in hydraulic efficiency caused by bubbles will damage the functional and structural integrities of tissues and cell components, and threaten life of the tree[7]. From observational evidence it is known that some plants are capable of removing embolisms[10, 35-37] to restore water
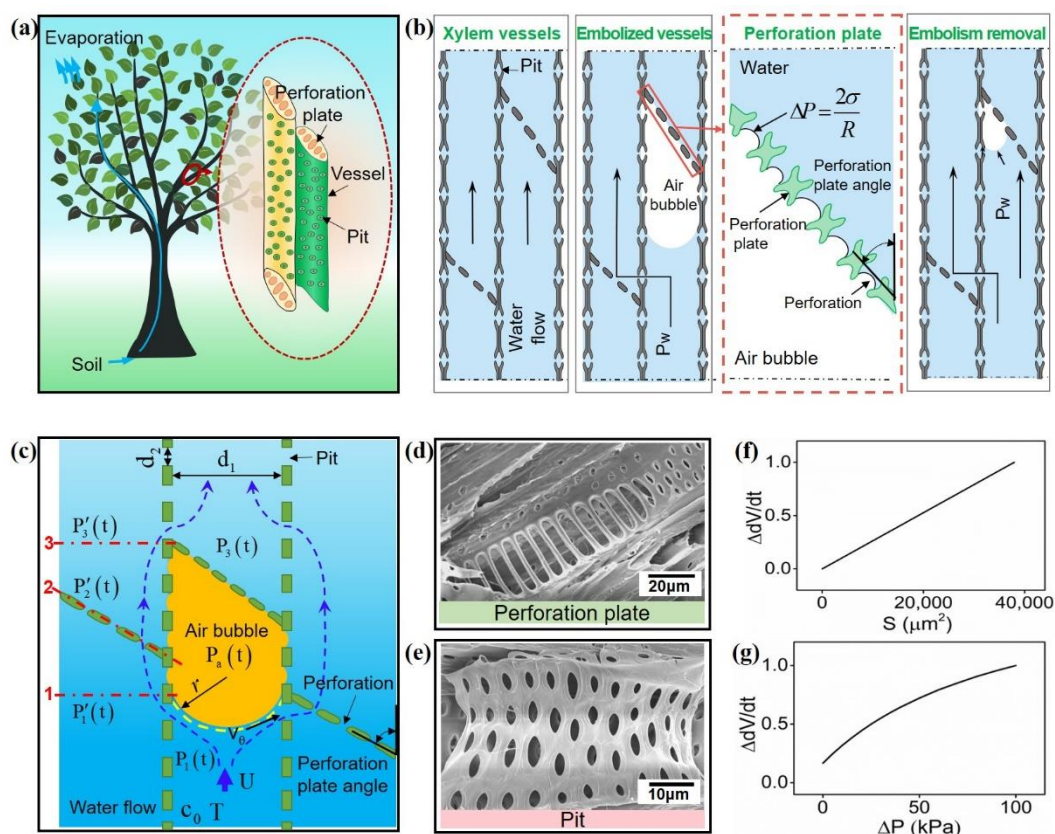

Figure 1 Schematic representation of embolism removal in angiosperm. a. Water transported in vessels from soil to leaves driven by transpiration. b. A vessel is blocked by an air bubble and air embolism forms. As water flows around the bubble and takes away the dissolved air, a gradual bubble dissolution process happens until the whole bubble disappears. c. The bubble dissolution model established to elucidate the mechanism of embolism removal. d. and e. SEM image of perforation plates and pits, respectively. f. The relationship between relative rate of embolism removal (Δ dV/dt) and gas-liquid interface area. Δ dV/dt was accessed by calculating the ratio between the rate of embolism removal and the maximum rate of embolism removal. g. The relationship between rate of embolism removal (Δ dV/dt) and pressure differential between the head and tail of the bubble.

transportation in vessels (Fig. 1b). This embolism removal occurs only when water is driven into the embolized vessels by means of an applied pressure gradient[38, 39]. In such a situation, pressure increased by the perforation plate facilitates the dissolution of air bubbles into the water stream, and the embolized vessels are refilled[31].

To study the micro-nano structures in vessels, the anatomical structure of the perforation plate (Fig. 1d) and pit (Fig. 1e) were examined in this research. Perforation plates are located at the connection between two vessel elements and pits are located within the walls between two adjacent vessels (Fig. 1b). The structure of a pit is that of a circular or an oval shaped hole when observed from the direction perpendicular to the surface of vessel wall. The perforation plate has many strip-shaped perforations. These perforations range from about 18 μm to 24 μm in length and are about 4 μm in width. The angle of the perforation plate to the perpendicular increases with the growth of vessel diameter[8]. On the basis of this information and other observed results, we can hypothesize that the perforation size and perforation plate angle influence the rate of embolism removal.

To elucidate the mass transfer mechanism of perforation plates in acceleration of embolism removal, a bubble dissolution model was established (Fig. 1c) based on the morphological characteristics of plant vessels. To simplify the structure and make it fit for analysis, the pits in this model were simplified to a circular shape and the perforations were simplified to a rectangle shape.

When an air bubble is held up in the vessel by a perforation plate, a curved gas-water interface is produced to prevent the air bubble from migrating to adjacent vessels. According to the Young–Laplace-Equation, the pressure differential that is enough to isolate neighboring vessels is:

$$\Delta P_a = \frac{2\sigma}{R_c}, \tag{1}$$

where R_c is the radius of curvature and σ is the surface tension force.

Water traversing a vessel that encounters a bubble could pass through nearby pits and enter adjacent vessels to continue water transportation. As water passes around the bubble and takes away any dissolved air, the bubble continues to reduce in size until it effectively disappears. The process of embolism removal can be explained by the mechanism of mass transfer. At constant temperature and pressure, the average molar flux of gas across the bubble surface is given by (Supplementary Note 1):

$$N_{\text{avg}} = \left(S_a - c_0\right)\sqrt{\frac{2D_{AB}U}{3\pi R}}, \tag{2}$$

where S_a is the solubility of air in water, c_0 is the equilibrium concentration of gas dissolved in water, D_{AB} is the diffusion

coefficient, U is the initial flow velocity and R is the equivalent radius of the air bubble.

For a stationary bubble boundary, the mass transferred from the bubble to the fluid per unit time is conserved:

$$\frac{dn_a}{dt} = c_a \frac{dV}{dt} = -N_{avg}S, \tag{3}$$

where n_a is the amount of substance of the bubble, t is the time variable, c_a is the molar concentration of the gas in the bubble, V is the bubble volume and S is the gas-liquid interface area.

According to Henry's law and the equation of state for an ideal gas, the change rate of the volume of the bubble can be achieved (Supplementary Note 1):

$$\frac{dV}{dt} = -\Re TS(K_H - \frac{c_0}{P_3 + \Delta P_w + \frac{2\sigma}{R}})\sqrt{\frac{2D_{AB}U}{3\pi R}}, \tag{4}$$

where $\Re$ denotes the universal gas constant, T is the liquid temperature, P_3 is the pressure at the head of the bubble, and ΔP_w is the pressure differential between the head and tail of the bubble.

$$\Delta P_w = 0.71\rho_w\left(1 - \frac{d_2^2}{d_1^2}\right)\left(\frac{4Q}{\pi d_2^2}\right) + \rho_w K \frac{v_\theta^2}{2} + \Delta P_p \tag{5}$$

where ρ_w is the density of water, d_1 and d_2 are the diameters of the vessel and pit, respectively, Q is the volume flow rate of water in the vessel and K is the local loss coefficient that depends on the bubble radius and the geometric parameters of adjacent vessels.

The pressure differential ΔP_w is affected by the structural parameters of the pits and vessels, bubble radius and the pressure differential $\mathrm{D}P_p$ caused by the perforation plate. We can conclude that the acceleration of embolism removal is imputable to the growth of gas-liquid interface area and increase of pressure differential and can therefore be attributed to the geometric parameters of the perforation plate.

Pressure differential $\mathrm{D}P_p$ increased by perforation plates

When water in the vessels passes through a perforation plate, the cross section of water reduces and its flow velocity increase, which results in energy loss and pressure drop. A pressure differential across the perforation plate is created. The increased pressure differential means that the perforation plate increases the flow resistance in the vessel and reduces the hydraulic efficiency.

By applying Bernoulli's equation and the continuity equation between sections 1, 2, and 3 in Fig.1c, the pressure differential caused by the perforation plate can be obtained,
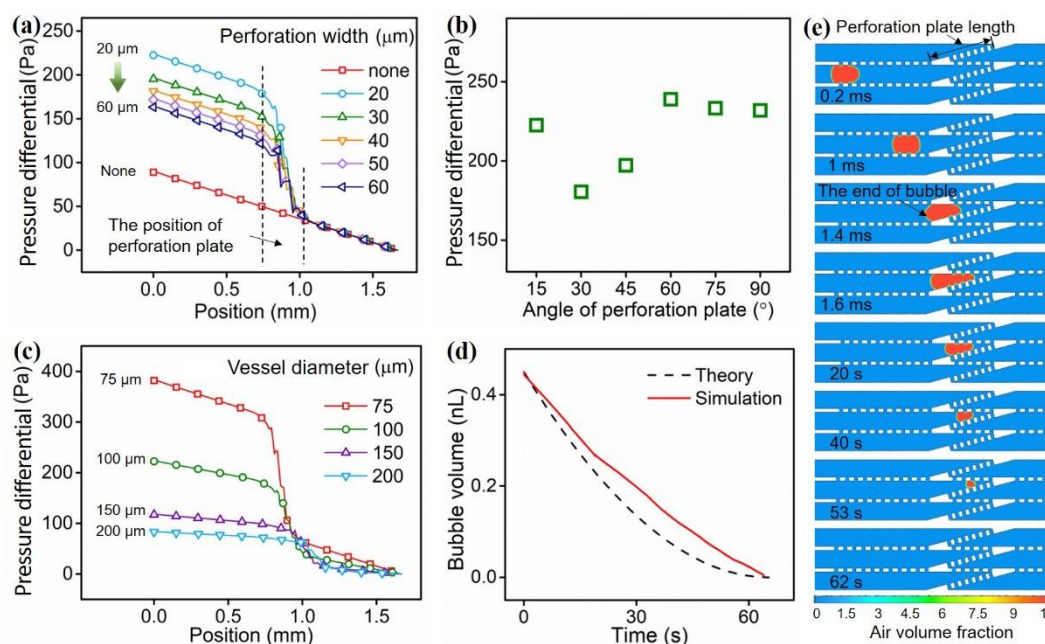
Figure 2 The effect of structural parameters of perforation plate on pressure differential. a. Simulation results of pressure differential with respect to the square perforation width (20 µm, 30 µm, 40 µm, 50 µm and 60 µm). b. Simulation results of pressure differential with respect to the angle of perforation plate (15°, 30°, 45°, 60°, 75° and 90°). c. Simulation results of pressure differential with respect to the vessel diameter (75 µm, 100 µm, 150 µm, 200 µm). d. Comparison of theoretical and simulated times of embolism removal. e. Simulation results of the bubble capture and embolism removal process in the vessel with perforation plates.

$$\Delta P_p = \xi \frac{\rho_w v_3^2}{2} + \rho_w g \left(z_3 - z_1 \right) + \lambda \rho_w \frac{\left(z_3 - z_1 \right) v_3^2}{2 d_1}, \qquad (6)$$

where g is the acceleration due to gravity, λ is the Darcy friction factor, v_3 is the average flow velocity at section 3, z_1 and z_3 are the heights of sections 1 and 3, respectively, ξ is the local resistance coefficient determined by the geometric parameters of perforation plate. From the anatomical structures of the perforation plates and equation (6), the parameters of perforation width, perforation plate angle and vessel diameter are considered the substantial parameters that affect pressure differential and embolism removal.

To confirm the influence of these geometric parameters of the perforation plate on pressure differential $\mathrm{D}P_p$, numerical simulations were carried out based on the morphological characteristics of plant vessels. To simplify the structure and make it fit for analysis, the perforations in this section of the work was simplified to a square shape.

As shown in Fig. 2a, compared with the vessel without perforation plates, the pressure differential between inlet and outlet shows a marked increase at the position of the perforation plate. The pressure differential across the perforation plate decreases with increase of the perforation width. The relationship between the angle of the perforation plate and the pressure differential was also simulated. Since the effective length of the perforation plate increases with decrease of the perforation plate angle, for the same perforation width, the number of perforations increases with decrease of the perforation plate angle. In the CFD model, when the angle of the perforation plate is 15°, 30°, 45°, 60°,

75° and 90°, the corresponding number of perforations are 7, 4, 3, 2, 2, and 2, respectively. As shown in Fig. 2b, the pressure differential across a perforation plate with an angle of 60° is higher than that for an angle of 75° and 90°. This result shows that, with the same number of perforations, the perforation plate with a smaller angle produces a higher pressure differential. However, with decrease of the perforation plate angle (from 60° to 30°), the pressure differential is reduced. This is because the number of perforations increases from 2 to 4 and the effective cross section of the flow area increases. In an extreme example, the perforation plate with an angle of 15° has a higher pressure differential than that for the perforation plate with an angle of 30°. This is because the effective cross section area of the perforation plate at an angle of 15° along the axis of the vessel is so small that the direction of water flow has to change significantly to traverse the perforated plate, which results in large energy loss. Simulation results of vessel diameter on flow resistance (Fig. 2c) show that, with the same perforation width and perforation plate angle, narrower vessels have a larger pressure differential, which aligns with the study that determined hydraulic resistance in vessels with scalariform perforation plate decreased with the increase of vessel diameter[20].

Simulations were also conducted to verify the influence of perforation plates on the process of embolism removal. Fig. 2e shows the bubble capture and removal process in the vessel with a perforation plate. In Fig. 2e, an air bubble is shown in red and water is shown in blue. During the simulation, when a bubble was introduced in a vessel, it was captured by the perforation plate. Water that flows past and against the bubble passes through nearby pits and flows into adjacent

vessels to continue transportation. As the water flows around the bubble and removes the dissolved air, the bubble reduces in mass and volume until it is fully or effectively dissolved. Fig. 2d shows the comparison of theoretical and simulated times of embolism removal under the condition of $\hat{A} = 287$, $T = 298\,K$, $a = 55°$, $D_{AB} = 1.89e^{-9}\,m^2/s$, $K_H = 2.02e^{-7}$ and $c_0 = 0.02\,mol/L$. The theoretical result agrees with the simulation one. The error between the simulation and theoretical model is because the end of bubble was simplified to an ideal hemispherical shape in the theoretical model, while the end of bubble was not an ideal hemisphere in simulation.

From equation (4) and the simulation results, important postulates can be presented:

(1) The perforation plates can increase the pressure differential in vessels and can improve the rate of embolism removal (Fig. 1g). Pressure differential is affected by the geometric parameters of the perforation plate and the vessel diameter. A combination of the size of the perforations, diameter of the vessel and the perforation plate angle can be optimised to generate higher pressure differential, which can accelerate the embolism removal.

(2) The rate of embolism removal increases with the growth of the effective gas-liquid interface surface area (Fig. 1f).

Microfluidic device replicating the vessels of plant

Although the simulations reported in Fig.2 demonstrate that the geometric parameters of the perforation plate and the vessel diameter can increase the pressure differential in vessels, it is not directly clear that they accelerate embolism removal. Due to the difficulty of performing standardised tests with different geometric parameters in plants, biomimetic devices inspired by vessels in angiosperm were designed and

fabricated and then used to carry out analysis to further verify the role that the perforation plates play in embolism removal of plants.

As shown in Fig. 3a and Supplementary Fig. S2, the biomimetic device consists of three parts: the channels mimicking the vessels of plant, the pits and the perforation plates. The channels are 10 mm-long, 30 μm-high and 100 μm-wide. A T-junction used to generate bubbles was set at the entrance of the device. To prevent particles and impurities from entering and interfering with the experimental results, filter units were set at the gas and liquid inlets. The assembled biomimetic device is show in Fig.3b. Two pressure sensors were used to measure the pressure differential between the location of pressure measurement hole and the outlet of the biomimetic device.

Because the contact angle between the water and the wall of the vessel ranges from 24.5° to 80.3° [8], the modified polydimethylsiloxane (PDMS) was used as the material of the biomimetic device in the experiment. Since plasma modification of PDMS is time-sensitive (Fig. 3c), to keep the water contact angle of the biomimetic device within a reasonable range, the modified devices were tested within 4 hours. When a bubble was injected into the biomimetic device, it was intercepted by the perforation plate. When such a scenario occurs, two things happen. Water changes its direction and passes through the pits to continue its transportation and the pressure differential, increased by the perforation plate, facilitates the dissolution of air bubbles into the water stream. The bubble dissolves gradually in the device under the hydraulic force (Fig. 3d and Movie S1).

To study the effect of geometric parameters of a perforation plate on embolism removal, perforation plates with perforation widths from 20 μm to 60 μm and perforation
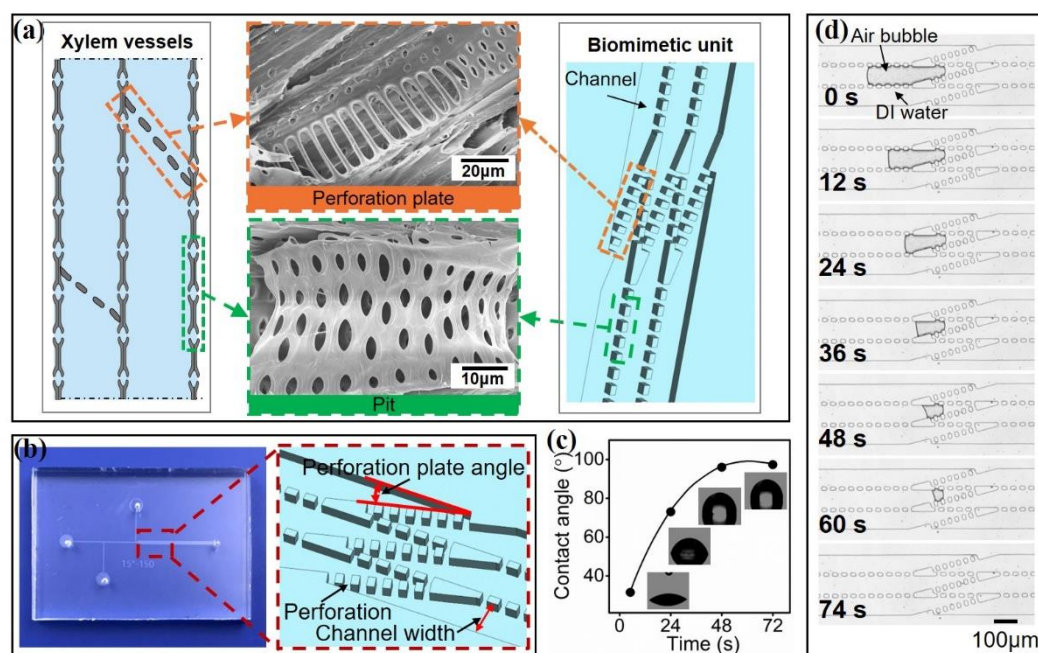

Figure 3 The biomimetic device used for evaluating the role that the perforation plates play in embolism removal. a. The diagram of the biomimetic device. b. Photograph of the assembled biomimetic device and a schematic diagram used to elucidate geometric parameters of the biomimetic device. c. Variation of water contact angle on hydrophilic modified PDMS with respect to time. d. The process of embolism removal in the biomimetic device.

plate angles from 15° to 90° (Supplementary Fig. S4 and S5) were designed and tested. To study the effect of perforation plates on embolism removal in vessels with different diameters, biomimetic devices with channel widths of 75 μm, 100 μm, 150 μm and 200 μm were fabricated and tested (Supplementary Fig. S6). To verify the essential role that the perforation plates play in the process of embolism removal, biomimetic devices without perforation plates were also designed and tested.

Microfluidic device for studying the mechanism by which perforation plates accelerate embolism removal

At a flow rate of 25 μL/min, the Reynolds number of flows in the biomimetic device was 2.1, which was similar to the Reynolds number (0.004-3.985) of the flow in vessels. Embolism removal experiments were carried out using the biomimetic devices with and without perforation plates. As shown in Fig. 4a, when there are no perforation plates, the embolism removal time is 137±9 s. When there are three perforation plates set at an angle of 15°, perforation spacing of 20 μm and channel width of 100 μm, the embolism removal times of the devices with perforation widths of 20 μm, 30 μm, 40 μm, 50 μm and 60 μm are 75±3 s, 77±5 s, 89±1 s and 95±2 s, respectively. The results show that perforation plates could facilitate the elimination of bubbles. The larger the perforation width the longer the time required for embolism removal. Compared with the biomimetic device without perforation plates, the removal rate of the bubble is improved by a factor
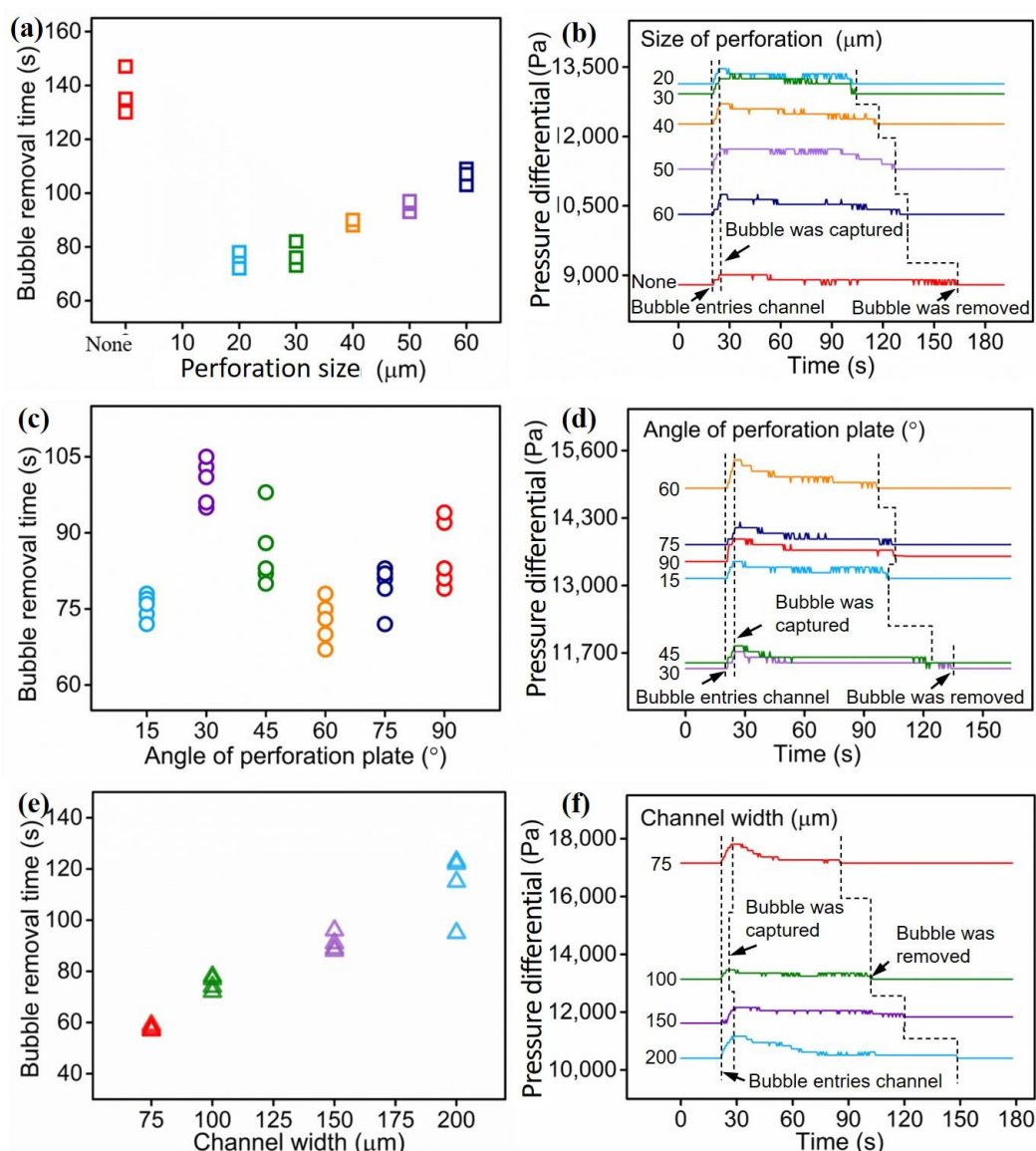

Figure 4 Embolism removal performance of the biomimetic device. a. Variation of embolism removal time with respect to the perforation width (20 μm, 30 μm, 40 μm, 50 μm and 60 μm). b. Variation of pressure differential with respect to the perforation width (20 μm, 30 μm, 40 μm, 50 μm and 60 μm). c. Variation of embolism removal time with respect to the angle of perforation plate (15°, 30°, 45°, 60°, 75° and 90°). d. Variation of pressure differential with respect to the angle of perforation plate (15°, 30°, 45°, 60°, 75° and 90°). e. Variation of embolism removal time with respect to the channel width (75 μm, 100 μm, 150 μm, 200 μm). f. Variation of pressure differential with respect to the channel width (75 μm, 100 μm, 150 μm, 200 μm).

of approximately 1.83. In the experiment, the pressure differential across the main channel during the entire embolism removal process was monitored (Fig. 4b). Before the bubble was injected into the channel, the pressure differential of the device with small perforation width is greater than that with large perforation width, which is consistent with the simulation results. When a bubble was injected into the biomimetic device, the pressure differential increased. As the bubble was captured by perforation plate, the pressure differential attains its maximum value. The bubble then steadily decreased in size in the channel. At the same time, the pressure differential decreased slowly until the bubble was removed. The pressure differential then returns to its initial level. In conclusion, a perforation plate with a smaller perforation width can generate a larger pressure differential and higher hydraulic resistance, which results in a higher rate of embolism removal.

Compared with the clear relation between perforation width and embolism removal time, the relationship between the angle of the perforation plate and embolism removal time is relatively complicated. As shown in Fig. 4c, in the biomimetic device with a perforation width of 20 μm and a channel width of 100 μm, the embolism removal times of the devices with perforation plate angles of 15°, 30°, 45°, 60°, 75° and 90° are 75±2 s, 100±4 s, 86±7s, 72±4 s, 79±4 s and 86±7 s, respectively. From 30° to 60°, embolism removal time decreases as the angle increases. That is because pressure differential increases as the angle increases (Fig. 4d). From 60° to 90°, time lengthens as the angle increases. That is because pressure differential decreases as the angle increases (Fig. 4d). With the perforation plate angle from 30° to 90°, the embolism removal time reduces with the increase of pressure differential. But the embolism removal time of 15° is shorter than that for an angle of 90° and 75°, which is inconsistent with the corresponding measure of pressure differential in the experiment (Fig. 4d). The reason is that the perforation plate with angle of 15° has more perforations and a larger gas-liquid interface area, which is conducive to the dissolution of air. Therefore, the process of embolism removal in vessels is a coupling result of the pressure differential across the vessel and the gas-liquid interface.

To test the effect of vessel diameter on embolism removal, experiments were conducted on biomimetic devices with different channel widths. As shown in Fig. 4e, with a perforation width of 20 μm and angle of 15°, the embolism removal times of the biomimetic device with channel widths of 75 μm, 100 μm, 150 μm and 200 μm are 58±1 s, 75±3 s, 91±4 s and 113±13 s, respectively. The pressure differentials across the biomimetic devices decrease with the increase of channel width, which is consistent with the simulation results (Fig. 4f).

The test results show that a perforation plate in the vessel could facilitate the process of embolism removal by increasing

flow resistance and gas-liquid interface. A perforation plate with a smaller perforation width, more perforations and a larger perforation angle can generate a larger pressure differential and higher hydraulic resistance, which results in a higher rate of embolism removal. But high hydraulic resistance and will decrease hydraulic efficiency. Due to the hydraulic resistance decrease with the increase of vessel diameter, the perforation plate with small angle distributed in the narrow vessel is beneficial to improve the hydraulic efficiency, and the perforation plate with large angle in the large vessel is helpful to increase the flow resistance and facilitate embolism removal. These results accord with the observation results in previous studies that the angle of a perforation plate increases with the growth of vessel diameter[8].

A perforation plate with a smaller perforation width, more perforations and a larger perforation angle can result in a higher rate of embolism removal. Previous study[14] show that a greater percentage of this kind of perforation plates is associated with smaller vessel diameters, shorter plant heights, and drier climates. Plant species with this kind of perforation plates can adapt to drought environment. The results in this article explain the reason why plants in drier climates have more perforation plates with small perforation width, more perforations and large perforation plate angle. These features can be used to screen drought-resistant plant.

Application of embolism removal in the determination of heavy metal ions

The mechanism by which perforation plates accelerate embolism removal in vessels can be applied to remove bubbles in the determination of heavy metal ions. In order to verify the feasibility of this idea, a bionic bubble removal unit based on the same principle was designed to detect heavy metal ions in water.

Heavy metal contamination in water is a global issue because of toxicity hazard to human health, even at trace levels of concentration. Heavy metal ions, such as mercury, lead and copper, at elevated concentrations can cause severe illness, including cancer[40, 41], cardiovascular disease[42, 43], nervous system impairment[44] and liver damage[45]. Therefore, effective, reliable and real time determination of heavy metal ions in water would be of great benefit. Electrochemical flow sensors have been developed to detect heavy metal ions in water in real time [46-48]. However, bubbles that enter the sensor can easily accumulate and grow, which will decrease the sensitivity of these devices and reduce accuracy of analysis results. For instance, nucleation and adhesion of bubbles on the surface of the electrode can reduce electrochemical active surface area and lead to an insufficient enrichment of ions which, as a result, reduces the measured concentration of heavy metal ions. Therefore, removing bubbles from the electrochemical flow sensor in real time is of great importance.
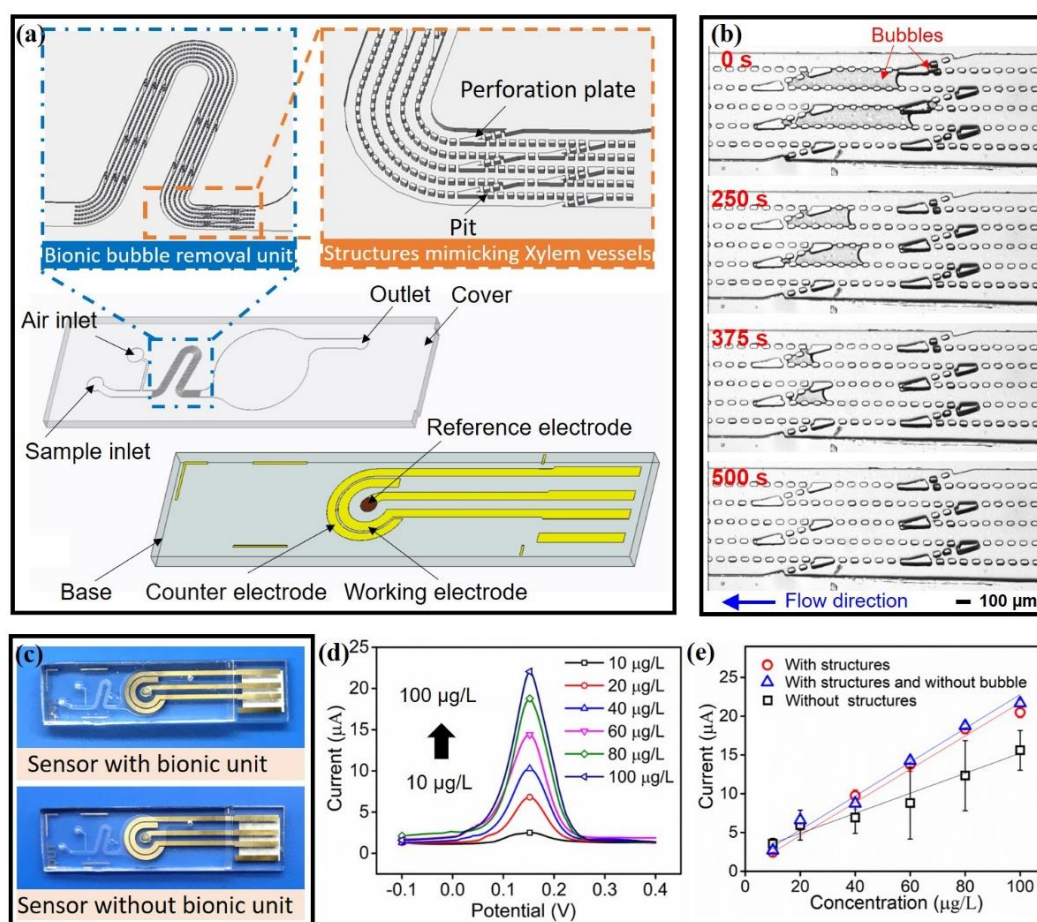
Figure 5 Electrochemical flow sensor integrated with a bionic bubble removal unit. a. The proposed electrochemical flow sensor. b. The bubble removal process in the bionic unit. c. The photographs of electrochemical flow sensor with/without bionic unit. d. Electrochemical responses of the sensor integrated with bionic unit at the concentration of Cu^{2+} from 10 μg/L to 100 μg/L. e. The standard calibration curve of the stripping peak current versus the concentration of copper ions of the sensor with or without the bubble removal unit. Measurement parameters: deposition potential of −0.05 V, deposition time of 70 s, amplitude of 25 mV and pulse width of 0.02s.

The bionic unit was designed and integrated in an electrochemical flow sensor (Fig. 5a) to measure the concentration of Cu^{2+}. In the experiment, Copper solution containing bubbles was injected into the microchannels to test the performance of the sensor. Constant pressure pump was used to introduce gas through the gas inlet, and precision syringe pump was used to introduce Cu^{2+} sample through the sample inlet. By controlling sample flow rate and the pressure of gas flow, bubbles with specific volume were formed by using the T-shaped channel. When injected into the microchannels, bubbles were intercepted by perforation plates and dissolved gradually (Fig. 5b and Movie S2). Moreover, when impurities or particles are stuck in the channel, the pits nearby can provide redundant channels, and the liquid is still able to flow and remove the bubbles. The bionic unit has the capability of filtering undesired particles/objects. As a contrast, an electrochemical flow sensor without the bionic unit was also fabricated and tested (Fig. 5c). When injected into the microchannels without the bionic unit, bubbles entered the sensor and accumulated in the detection area.

Differential pulse anodic stripping voltammetry (DPASV) was employed to measure the concentration of copper ions in the solution. Electrochemical responses of the sensor integrated with the bionic unit for concentrations of Cu^{2+} from 10 μg/L to 100 μg/L are illustrated in Fig. 5d. The current peak is located around 0.15 V with respect to the potential of the Ag/AgCl reference electrode.

Fig. 5e shows the calibration curve of peak current versus concentration of copper ions tested by using the electrochemical flow sensor with and without the bionic unit under bubble condition. The electrochemical flow sensor with bionic unit under no bubble condition was also tested as a contrast. Under bubble condition, for the electrochemical flow sensor with the bionic unit, the sensitivity and the limit of detection (LOD) are 0.214 μA/μg/L and 2.69 μg/L, respectively. Under no bubble condition, for the sensor with the bionic unit, the sensitivity and the LOD are 0.218 μA/μg/L and 2.64 μg/L, respectively. The results indicate that the influence of bubble removal process on the sensitivity and the limit of detection (LOD) of the sensor with the bionic unit is less than 1%. Under bubble condition, for the sensor without the bubble removal unit, the sensitivity and the LOD are 0.129 μA/μg/L and 13.02 μg/L, respectively. The sensitivity of the sensor with bionic unit is improved by a factor of 1.66 and the LOD is improved by a

factor of 4.84. The concentration error of copper ions measured by the electrochemical flow sensor with the bionic unit is much less than that of the electrochemical flow sensor without the bionic unit. It is because nucleation and adhesion of bubbles on the surface of the electrode reduce electrochemical active surface area and lead to an insufficient enrichment of Cu2+ which, as a result, reduces the measured concentration of Cu2+. Therefore, current response of the electrochemical flow sensor without the bionic unit is weak and its accuracy of analysis results is decreased. The test results suggest that the bionic unit can effectively eliminate bubbles and maintain the performance of the electrochemical flow sensor. Electrochemical flow sensors integrated with bubble removal units can be used for on-site determination of copper ions in water. The mechanism by which perforation plates accelerate embolism removal can be applied in the engineering field to help solve the problems of decrease of sensitivity, inaccuracy of analysis results and poor reaction performance caused by bubbles.

Conclusion

This work proposes a mathematical model and a biomimetic microfluidic device to study the mechanism of perforation plates of vessels in the acceleration of embolism repair. The mechanism by which perforation plates accelerate the process of embolism removal was explained detailly. The relationship between the rate of embolism removal and the pressure differential produced by perforation plates has been demonstrated. Simulations presented the influence of the structural parameters of a perforation plate on the pressure differential. Experiments verified the relationship between the structural parameters of a perforation plate and embolism removal performance.

The first conclusion of this article is perforation plates facilitate embolism removal by increasing the pressure differential and the gas-liquid interface area, and the rate of embolism removal is related to the structural parameters of perforation plate. According to equation (4), the rate of embolism removal in a vessel is related to the gas-liquid interface area and the pressure differential between the head and tail of the bubble. The gas-liquid interface area and the pressure differential are affected by certain geometric parameters of the perforation plate and vessel diameter. These parameters can be optimised to generate a higher pressure differential, which can accelerate the embolism removal. But increasing pressure differential will magnify flow resistance which, in turn, can reduce the hydraulic efficiency of water transportation in the vessels. Therefore, practical geometric parameters of perforation plate in plant is a nature balance of embolism removal performance and hydraulic efficiency.

According to the simulation and experiment results, a small perforation plate angle can reduce flow resistance by increasing flow area, while large angle can increase flow resistance and facilitate embolism removal. What's more, narrow vessel can increase the flow resistance and speed up the process of embolism removal. In narrow vessels, flow resistance is higher and is better able to ensure the rate of embolism removal. A perforation plate with a small angle is beneficial to promote hydraulic efficiency while in large vessels, hydraulic efficiency is high and a perforation plate with large angle can increase the rate of embolism removal by increasing flow resistance.

The second conclusion is that the process by which perforation plates accelerate embolism removal can be applied to a practical setting. In this article, the mechanism was applied to the bubble elimination in an electrochemical flow sensor for real time determination of heavy metal ions, which paves the way for applying the theory to practical settings. The test results suggest that a bionic unit can effectively maintain the sensitivity of an electrochemical flow sensor by eliminating bubbles. An electrochemical flow sensor integrated with a bubble removal unit can be used for on-site determination of copper ions in water. The mechanism can be applied in the water management engineering field to solve the problem of reduced sensitivity of such devices, inaccuracy of analysis results and poor reaction performance caused by bubbles.

Author contributions

G.L.H. and L.J.M. were involved in the conceptualization. L.Y.C. was involved in the scientific considerations. G.L.H. and L.L. were involved in the treatment of plant tissue, device fabrication and experimental set-up. G.L.H. performed the experiments, data analysis, interpretation, and statistical analysis. G.L.H contributed to the writing – original draft. L.Y.C. contributed to the writing–review & editing. L.C. provided expertise in the work.

Conflicts of interest

There are no conflicts of interest to declare.

Acknowledgements

Reference

1.   W. R. L. Anderegg, C. Schwalm, F. Biondi, J. J. Camarero, G. Koch, M. Litvak, K. Ogle, J. D. Shaw, E. Shevliakova, A. P. Williams, A. Wolf, E. Ziaco and S. Pacala, *Science*, 2015, **349**, 528-532.

2. W. M. Hammond, A. P. Williams, J. T. Abatzoglou, H. D. Adams, T. Klein, R. Lopez, C. Saenz-Romero, H. Hartmann, D. D. Breshears and C. D. Allen, *Nature Communications*, 2022, **13**.

3. P. Mahdavi, H. G. Kharazi, H. Eslami, N. Zohrabi and M. Razaz, *Water Supply*, 2021, **21**, 899-917.

4. M. A. Zwieniecki and N. M. Holbrook, *Trends Plant Sci.*, 2009, **14**, 530-534.

5. I. F. Cuneo, F. Barrios-Masias, T. Knipfer, J. Uretsky, C. Reyes, P. Lenain, C. R. Brodersen, M. A. Walker and A. J. McElrone, *New Phytol.*, 2021, **229**, 272-283.

6. A. Nardini, M. A. Lo Gullo, P. Trifilo and S. Salleo, *Environ. Exp. Bot.*, 2014, **103**, 68-79.

7. S. Souden, M. Ennajeh, S. Ouledali, N. Massoudi, H. Cochard and H. Khemira, *Trees-Structure and Function*, 2020, **34**, 1439-1452.

8. C. R. Brodersen, T. Knipfer and A. J. McElrone, *New Phytol.*, 2018, **217**, 117-126.

9. J. S. Sperry, N. M. Holbrook, M. H. Zimmermann and M. T. Tyree, *Plant Physiol.*, 1987, **83**, 414-417.

10. C. R. Brodersen and A. J. McElrone, *Front. Plant Sci.*, 2013, **4**.

11. M. Y. Ogasa, H. Taneda, H. Ooeda, A. Ohtsuka and E. Maruta, *Tree Physiol.*, 2019, **39**, 1725-1735.

12. T. Knipfer, I. F. Cuneo, C. R. Brodersen and A. J. McElrone, *Plant Physiol.*, 2016, **171**, 1024-1036.

13. S. Carlquist, *Botany*, 2012, **90**, 901-940.

14. J. S. Medeiros, F. Lens, H. Maherali and S. Jansen, *New Phytol.*, 2019, **221**, 1802-1813.

15. C. R. Brodersen, A. J. McElrone, B. Choat, M. A. Matthews and K. A. Shackel, *Plant Physiol.*, 2010, **154**, 1088-1095.

16. B. G. Hwang, J. Ryu and S. J. Lee, *Front. Plant Sci.*, 2016, **7**.

17. J. Hong, S. Liu, P. Glover, S. Wu and Y. Yan, *J. Bionic Eng.*, 2017, **14**, 622-630.

18. M. Y. Ogasa, K. Yazaki, Y. Utsumi, N. H. Miki and K. Fukuda, *Tree Physiol.*, 2019, **39**, 1685-1695.

19. S. Trueba, S. Delzon, S. Isnard and F. Lens, *J. Exp. Bot.*, 2019, **70**, 3227-3240.

20. M. A. Christman and J. S. Sperry, *Plant Cell and Environment*, 2010, **33**, 431-443.

21. J. Ryu, B. G. Hwang and S. J. Lee, *Ann. Bot.*, 2016, **118**, 1033-1042.

22. V. Rolland, D. M. Bergstrom, T. Lenne, G. Bryant, H. Chen, J. Wolfe, N. M. Holbrook, D. E. Stanton and M. C. Ball, *Plant Physiol.*, 2015, **168**, 1636-1647.

23. J. Sperry, *Plant Cell and Environment*, 2013, **36**, 1916-1918.

24. M. D. Venturas, E. D. MacKinnon, A. L. Jacobsen and R. B. Pratt, *Plant Cell and Environment*, 2015, **38**, 1060-1068.

25. J. K. Wheeler, B. A. Huggett, A. N. Tofte, F. E. Rockwell and N. M. Holbrook, *Plant Cell and Environment*, 2013, **36**, 1938-1949.

26. J. S. Sperry, *Plant Physiol.*, 1986, **80**, 110-116.

27. J. S. Sperry, *Int. J. Plant Sci.*, 2003, **164**, S115-S127.

28. H. K. Kim and S. J. Lee, *New Phytol.*, 2010, **188**, 1085-1098.

29. S. J. Lee, B. G. Hwang and H. K. Kim, *Planta*, 2013, **238**, 307-315.

30. S. J. Lee and Y. Kim, *Ann. Bot.*, 2008, **101**, 595-602.

31. S. J. Lee, J. Park and J. Ryu, *Front. Plant Sci.*, 2019, **9**.

32. S. Delzon and H. Cochard, *New Phytol.*, 2014, **203**, 355-358.

33. F. Y. Shen, R. F. Gao, W. J. Liu and W. J. Zhang, *Tree Physiol.*, 2002, **22**, 655-659.

34. H. J. Schenk, S. Espino, D. M. Romo, N. Nima, A. Y. T. Do, J. M. Michaud, B. Papahadjopoulos-Sternberg, J. Yang, Y. Y. Zuo, K. Steppe and S. Jansen, *Plant Physiol.*, 2017, **173**, 1177-1196.

35. I. F. Cuneo, T. Knipfer, P. Mandal, C. R. Brodersen and A. J. McElrone, *New Phytol.*, 2018, **218**, 506-516.

36. D. M. Love and J. S. Sperry, *Tree Physiol.*, 2018, **38**, 1006-1015.

37. P. Trifilo, N. Kiorapostolou, F. Petruzzellis, S. Vitti, G. Petit, M. A. Lo Gullo, A. Nardini and V. Casolo, *Plant Physiol. Biochem.*, 2019, **139**, 513-520.

38. K. H. Jensen, K. Berg-Sorensen, H. Bruus, N. M. Holbrook, J. Liesche, A. Schulz, M. A. Zwieniecki and T. Bohr, *Rev. Mod. Phys.*, 2016, **88**.

39. M. D. Venturas, J. S. Sperry and U. G. Hacke, *J. Integr. Plant Biol.*, 2017, **59**, 356-389.

40. H. Satoh, *Ind. Health*, 2000, **38**, 153-164.

41. J. F. Risher and S. N. Amler, *Neurotoxicology*, 2005, **26**, 691-699.

42. T. A. Sheikh, M. N. Arshad, M. M. Rahman, A. M. Asiri and K. A. Alamry, *J. Organomet. Chem.*, 2016, **822**, 53-61.

43. M. R. Rahimzadeh, M. R. Rahimzadeh, S. Kazemi and A. A. Moghadamnia, *Caspian Journal of Internal Medicine*, 2017, **8**, 135-145.

44. M. Vilar, J. Barciela, S. Garcia-Martin, R. M. Pena and C. Herrero, *Talanta*, 2007, **71**, 1629-1636.

45. M. W. Fitch, D. W. Graham, R. G. Arnold, S. K. Agarwal, P. Phelps, G. E. Speitel and G. Georgiou, *Appl. Environ. Microbiol.*, 1993, **59**, 2771-2776.

46. J. F. van Staden and M. C. Matoetoe, *Anal. Chim. Acta*, 2000, **411**, 201-207.

47. H. Panagopoulou, A. Economou and C. Kokkinos, *Anal. Chim. Acta*, 2021, **1159**.

48. B. Ninwong, S. Chuanuwatanakul, O. Chailapakul, W. Dungchai and S. Motomizu, *Talanta*, 2012, **96**, 75-81.